

Finite element analysis of V-ribbed belts using neural network based hyperelastic material model

Y. Shen^a, K. Chandrashekhara^{a,*}, W.F. Breig^b, L.R. Oliver^b

^a*Department of Mechanical and Aerospace Engineering and Engineering Mechanics, University of Missouri-Rolla, Rolla, MO 65409, USA*

^b*MarkIV Automotive, Springfield, MO 65808, USA*

Received 5 May 2003; received in revised form 30 September 2004; accepted 14 October 2004

Abstract

A three-dimensional finite element model was built to study V-ribbed belt pulley contact mechanics. The model consists of a pulley and a segment of V-ribbed belt in contact with the pulley. A material model for the belt, including the rubber compound and the reinforcing cord is developed. Rubber is modeled as hyperelastic material. The hyperelastic strain energy function is approximated by neural network trained by rubber test data. Reinforcing cord is modeled as elastic rebar. The material model developed is implemented in the commercial finite element code ABAQUS to simulate the V-ribbed belt-pulley system. A study is then conducted to investigate the effect of belt pulley system parameters on the contact mechanics. The effects of temperature and aging on belt materials are also investigated. The information gained from the analysis can be applied to optimize V-ribbed belt and pulley design.

© 2004 Elsevier Ltd. All rights reserved.

Keywords: Belt; Contact; Finite element; Hyperelastic material; Neural network

1. Introduction

V-ribbed belt drive systems have become increasingly important to the automotive industry since their introduction in the late 1970s. They provide an efficient means of transmitting power to all accessories. V-ribbed belt drive systems have proven advantages of compact mounting space, smaller pulley diameters,

capability of backside operation, and longer life. Consequently there is a need to understand the operational characteristics of these belt drive systems for optimal design and manufacturing.

Belt drive mechanics was first investigated by Euler [1]. He established the relationship between belt tension and coefficient of friction. Reynolds [2] developed the creep theory to explain the speed loss in power transmission belts. Firbank [3] proposed that creep theory did not provide an accurate representation of belt speed loss for belts contain reinforcement strands based on the fact that reinforced belts are practically inextensible. He came up with the shear theory, which

* Corresponding author. Tel.: +1 573 341 4587;
fax: +1 573 341 6899.

E-mail address: chandra@umr.edu (K. Chandrashekhara).

stated that the speed loss was mainly caused by the shear deformation of the belt section in contact with the pulley. Alciatore et al. [4] compared the creep and shear theory and concluded that shear theory are more applicable to reinforced belts. Gerbert [5] did thorough investigation on belt slip and proposed a unified approach to analyze belt slip in flat, V and V-ribbed belts.

The mechanics of V-ribbed belts has been studied by several researchers. Amijima et al. [6] described the relation between rib shear deformation and transmitted force. Hansson [7] did some experiment on V-ribbed belts and found that the belt slip decreased after a period of belt running time. This effect has been explained by the change in the belt rib profile and rib surface properties, which may increase the friction coefficient between belt and pulley. Yu et al. [8] examined the development of belt wear and found that the wear speed is fast initially and become stable after some running time. Tabatabaei [9] experimentally investigated the belt rib bottom and pulley groove tip contact and found that the traction capacity was reduced by the contact. Tabatabaei [10] also did a theoretical modeling on V-ribbed belt drives and came up with a new modification to Euler's equation, which gave the relationship between belt tension and coefficient of friction. Gerbert [5] did a lot of investigations on the mechanics of V-ribbed belts. His unified slip theory is the most extensive analytical model to predict belt slip.

Hansson [7] developed the first published finite element model of a V-ribbed belt system. His work investigated the effects of belt curvature on the wedge angle of the belt ribs and the contact pressures between belt ribs and pulley grooves. Yu et al. [8] presented a three-dimensional static model of a complete belt half-rib operating between two pulleys represented by rigid surfaces. The belt elastomer compound was modeled using an adapted form of the Ogden material model with the reinforcing cord modeled within a layer of cord-elastomer compound elements. They investigated belt pulley slip and stick, and found that a driving pulley has more severe contact than a driven pulley. Yu et al. [8] also presented a two-dimensional static model to investigate the effects of belt wear and wear debris on the belt-rib/pulley-groove pressure in a manner similar to that of Hansson [7]. Connell and Rorrer [11] also used two-dimensional finite element models to

determine the resonant frequencies of belt structures through modal analysis. Sloan et al. [12] developed a three-dimensional model to predict out of plane forces and displacements.

To better simulate V-ribbed belt drive system, it is necessary to build a three-dimensional finite element model with a fine finite element mesh and a satisfactory material model for the rubber compounds in the belts. In this work, a neural network based hyperelastic material model is presented. It is found to have more accurate curve fitting performance than the available strain energy functions. The neural network based material model is implemented in a finite element model to study belt pulley contact mechanics such as belt slip, belt rib pressure distribution, belt transmission efficiency, etc. A study is carried out to investigate the effects of belt drive parameters on belt drive system such as belt pulley size and belt rib and pulley groove wedge angle. The temperature and aging effects on the properties of rubber compounds are also studied. Their effects on the belt pulley contact are investigated.

2. Material model

The basic shape of a V-ribbed belt and its dimensions are shown in Fig. 1. These belts are a hybrid of V-belts and flat belts, offering the flexibility of a flat belt combined with the tracking and power transmission capacity of a V-belt. The main belt constituents consist of polyester cords as the tension-carrying member, a cushion elastomer compound that envelopes the cords and a fiber reinforced rib elastomer compound that forms the belt ribs.

The primary difficulty in simulating a belt is the rubber nonlinearity and the composite nature of a belt composed of multiple materials such as polyester cord and fiber filled rubber. Typically at strains larger than 5% the rubber compound becomes nonlinear elastic, characterized as hyperelastic. A strain energy function is needed to build the constitutive relation for a hyperelastic material. There are several strain energy function forms available in commercial finite element packages such as polynomial form [13] and Ogden form [14]. They have some constants to be determined by doing curve fitting of the rubber test data. From authors' experience, it needs much effort to obtain a

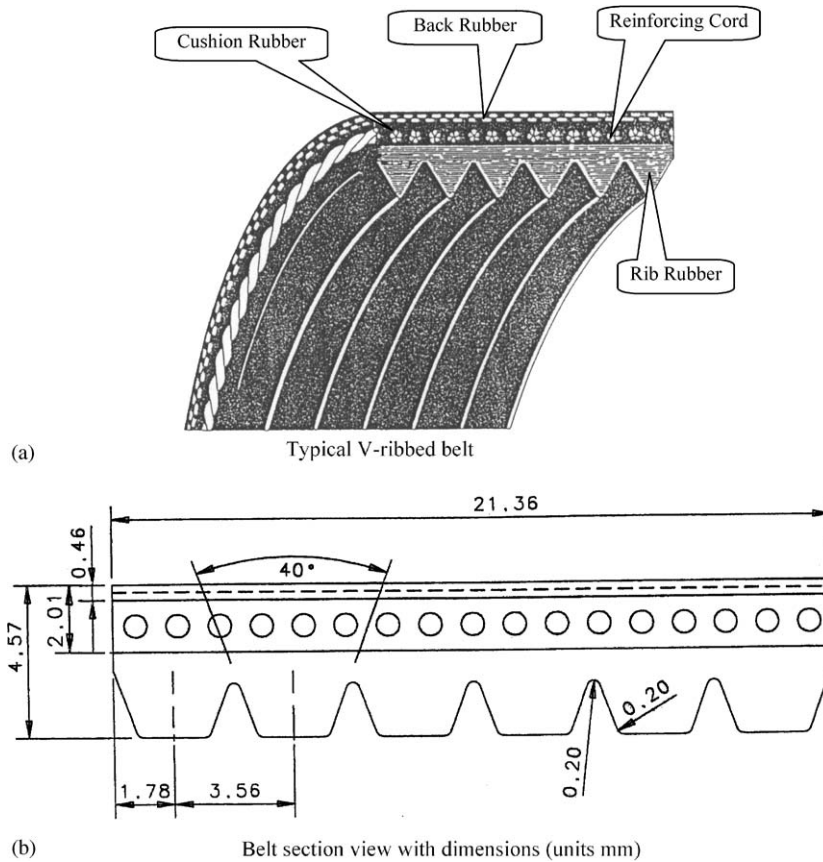


Fig. 1. Typical V-ribbed belt and its sectional dimension.

satisfactory curve fitting with the available strain energy functions. A new way of defining the strain energy function by using neural network is presented and it is found to give more accurate curve fitting results than the available strain energy functions. The neural network based strain energy function is described in the following sections.

3. Stress–strain relationship from strain energy function

In this section, the stress–strain relationship is developed for a general strain energy function based on strain invariants. Following ABAQUS [15] conventions, the first and second strain invariants \bar{I}_1 , \bar{I}_2 and volume ratio J are chosen as the variables in the strain

energy function. They are defined as:

$$\begin{aligned}\bar{I}_1 &= \bar{\lambda}_1^2 + \bar{\lambda}_2^2 + \bar{\lambda}_3^2, \\ \bar{I}_2 &= \bar{\lambda}_1^2 \bar{\lambda}_2^2 + \bar{\lambda}_2^2 \bar{\lambda}_3^2 + \bar{\lambda}_1^2 \bar{\lambda}_3^2, \\ \bar{\lambda}_k &= J^{-1/3} \lambda_k, \quad k = 1, 2, 3,\end{aligned}\quad (1)$$

where λ_k ($k = 1 \sim 3$) is the principle stretch ratios. The strain energy function can be expressed in terms of \bar{I}_1 , \bar{I}_2 and J , i.e.,

$$U = U(\bar{I}_1, \bar{I}_2, J). \quad (2)$$

To define the stress–strain behavior, some definitions and basic kinematic results are introduced. Writing the current position of a material point as \mathbf{x} (bold character represents vectors or matrices) and the reference position of the same point as \mathbf{X} , the deformation

gradient is then defined as

$$\mathbf{F} = \frac{\partial \mathbf{x}}{\partial \mathbf{X}} = \frac{\partial x_i}{\partial X_j} \quad (i, j = 1, 2, 3). \quad (3)$$

Then J , the total volume change at the point, is

$$J = \det(\mathbf{F}). \quad (4)$$

For simplicity, the deformation gradient with the volume change eliminated is defined as

$$\bar{\mathbf{F}} = J^{-\frac{1}{3}} \mathbf{F}. \quad (5)$$

Then, the deviatoric stretch matrix (the left Cauchy–Green strain tensor) of $\bar{\mathbf{F}}$ is introduced as

$$\bar{\mathbf{B}} = \bar{\mathbf{F}} \cdot \bar{\mathbf{F}}^T. \quad (6)$$

So that the first strain invariant is given by

$$\bar{I}_1 = \text{trace} \bar{\mathbf{B}} = \bar{B}_{ii} \quad (i = 1, 2, 3) \quad (7)$$

and the second strain invariant is given by

$$\begin{aligned} \bar{I}_2 &= \frac{1}{2} \left\{ (\text{trace}(\bar{\mathbf{B}}))^2 - \text{trace}(\bar{\mathbf{B}} \cdot \bar{\mathbf{B}}) \right\} \\ &= \frac{1}{2} \left\{ (\bar{B}_{ii})^2 - B_{ij} B_{ji} \right\}. \end{aligned} \quad (8)$$

The definition of \bar{I}_1 and \bar{I}_2 is equivalent to Eq. (1).

Then the stresses associated with the strain energy function are given by

$$\begin{aligned} \boldsymbol{\sigma} &= \frac{2}{J} \text{dev} \left\{ \left(\frac{\partial U}{\partial \bar{I}_1} + \bar{I}_1 \frac{\partial U}{\partial \bar{I}_2} \right) \bar{\mathbf{B}} - \frac{\partial U}{\partial \bar{I}_2} \bar{\mathbf{B}} \cdot \bar{\mathbf{B}} \right\} \\ &\quad + \frac{\partial U}{\partial J} \mathbf{I}, \end{aligned} \quad (9)$$

where dev means deviatoric and is calculated as $\text{dev}(\mathbf{A}) = \mathbf{A} - 1/3 \text{trace}(\mathbf{A})$ for matrix \mathbf{A} . \mathbf{I} is the Identity matrix. The first term is the deviatoric stress and second term is the hydrostatic pressure.

For incompressible material, $J = 1$, U is a function of \bar{I}_1 and \bar{I}_2 only. The hydrostatic pressure cannot be calculated by $\frac{\partial U}{\partial J}$. The stresses can be obtained by using penalty methods in finite element analysis [16].

4. Approximation of strain energy function by feedforward neural network

As discussed above, it needs much effort to obtain a good curve fitting with the available strain energy functions, especially when the rubber material is under small or large strain, say $\lambda < 0.3$ or $\lambda > 2.5$. The unsatisfactory curve fitting results come from the phenomenological approach. Because a strain energy form is firstly arbitrarily chosen, and then it is used to fit the rubber stress–strain curve which may not follow the relationship dictated by the chosen strain energy function.

In this work, a different logic in deciding the strain energy function is adopted. The energy function is not prescribed at first, but is fully determined by the rubber test data. This is made possible by the capability of the feedforward neural network to accurately approximate the nonlinear strain energy function and its partial derivatives according to the strain invariants and volume ratio [17]. The test data are collected at first. Then they are used to train a feedforward neural network. After the training process converges, the neural network can represent the strain energy function of the rubber material. Although the number of neurons and the initial weights are chosen arbitrarily before training, but they can be adjusted easily during the training process to follow the rubber test data. Thus the strain energy described by the neural network is fully determined by the test data.

Fig. 2 is an illustration of feedforward neural network used in this work. It has one input layer, one hidden layer and one output layer. The inputs to the neural network are \bar{I}_1 , \bar{I}_2 , the two strain invariants, and J , the volume strain ratio. The output is the corresponding strain energy. The W s and B s are the weights and biases of the neural network. They are determined by the training process. The activation function of the hidden layer is the log sigmoid function given by

$$f(x) = \frac{1}{1 + e^{-x}}. \quad (10)$$

It's derivatives are given by

$$f'(x) = \left(\frac{1}{1 + e^{-x}} \right)' = f(x)[1 - f(x)],$$

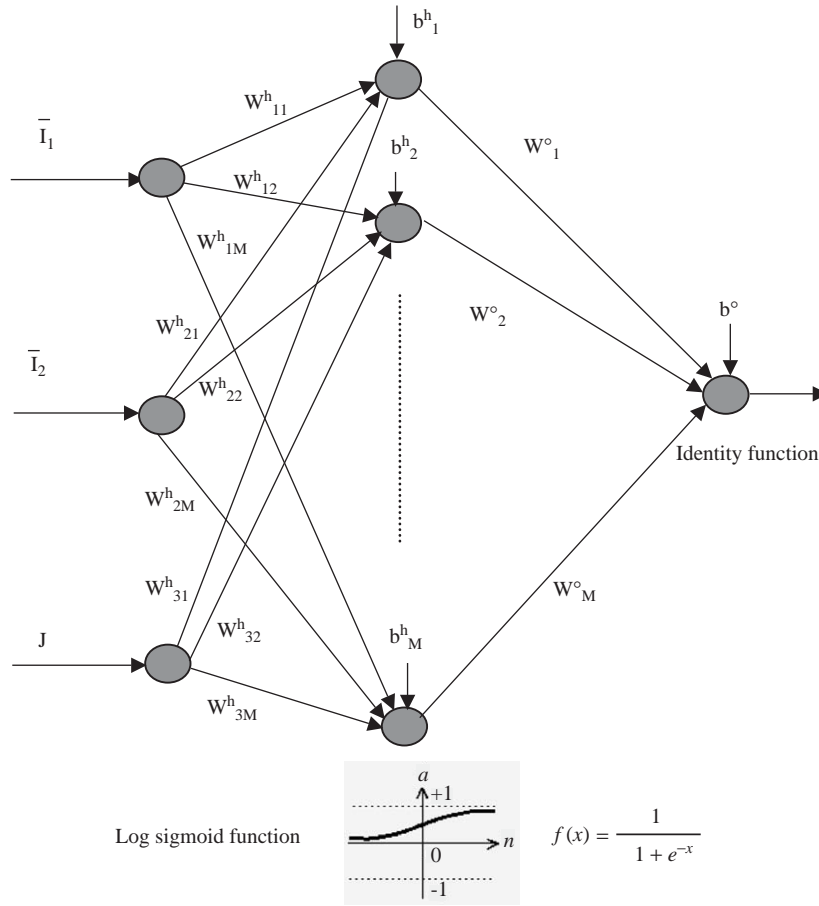


Fig. 2. Structure of the feed forward neural network.

$$\begin{aligned}
 f''(x) &= \left(\frac{1}{1 + e^{-x}} \right)'' \\
 &= f(x)[1 - f(x)][1 - 2f(x)], \\
 f'''(x) &= \left(\frac{1}{1 + e^{-x}} \right)''' \\
 &= f(x)[1 - f(x)] \\
 &\quad \times [1 - 6f(x) + 6(f(x))^2].
 \end{aligned} \quad (11)$$

The activation function for the output layer is the Identity function.

Thus, given the inputs \bar{I}_1 , \bar{I}_2 , and J , the strain energy is given by

$$U = \sum_{j=1}^M W_j^o f(O_j) + b^o, \quad (12)$$

where M is the number of neurons in the hidden layer, O_j is given by

$$O_j = \{\bar{I}_1, \bar{I}_2, J\} \begin{Bmatrix} W_{1j}^h \\ W_{2j}^h \\ W_{3j}^h \end{Bmatrix} + b_j^h, \quad (13)$$

W_j^o ($j=1, M$), W_{ij}^h ($i=1, 3, j=1, m$) are the weights of the neurons and b^o and b_j^h ($j=1, M$) are the biases as shown in Fig. 1.

The first derivatives of U can be calculated as (no summation rule)

$$\frac{\partial U}{\partial x_i} = \sum_{j=1}^M W_j^o W_{ij}^h f'(O_j), \quad (i=1, 2, 3), \quad (14)$$

where $x_1 = \bar{I}_1$, $x_2 = \bar{I}_2$, $x_3 = J$.

The second derivatives of U are given by

$$\frac{\partial^2 U}{\partial x_i \partial x_k} = \sum_{j=1}^M W_j^o W_{ij}^h W_{kj}^h f''(O_j), \quad (i, k = 1, 2, 3) \quad (15)$$

and the third derivatives of U are given by

$$\frac{\partial^3 U}{\partial x_i \partial x_k \partial x_l} = \sum_{j=1}^M W_j^o W_{ij}^h W_{kj}^h W_{lj}^h f'''(O_j), \quad (i, k, l = 1, 2, 3). \quad (16)$$

The first derivatives are required to calculate the Cauchy stress for a given strain state. The second and third derivatives are needed if ABAQUS/Standard user subroutine UHYPER is used to implement the hyper-elastic material model. For incompressible material, U is a function of \bar{I}_1 and \bar{I}_2 only. The inputs to the neural network are \bar{I}_1 and \bar{I}_2 . The derivatives of U according to J are set to zero in ABAQUS subroutine UHYPER. The calculation of the strain energy and its derivatives is the same except that O_j is given by

$$O_j = \{\bar{I}_1, \bar{I}_2\} \cdot \left\{ \begin{matrix} W_{1j}^h \\ W_{2j}^h \end{matrix} \right\} + b_j^h. \quad (17)$$

The neural network is trained using the rubber test data from simple tension, equi-biaxial tension and planar tension (also called pure shear) experiments. The inputs of the training data are strain invariants \bar{I}_1 , \bar{I}_2 and volume ratio J and the desired outputs are the corresponding strain energy. When collecting rubber hyper-elasticity test data to train the neural network, some practical issues should be considered. Fig. 3 shows a typical stress–strain curve for a rubber compound undergoing cyclic stretching. It is extended to 10% strain then returns to zero stress state. After several cycles, the maximum strain level is increased to 20%, followed by 30%, and at last a maximum strain of 100%. It can be seen from the figure that rubber softens at the first several load cycles. Each time when rubber material is stretched to a higher strain level, additional softening occurs after several load cycles. This effect is called strain softening. When collecting test data from experiments to determine the constants in the hyper-elastic strain energy function; one needs to estimate the maximum strain occurs in the rubber component and select the test data under the assumed strain level. Iteration may be needed to determine the appropriate

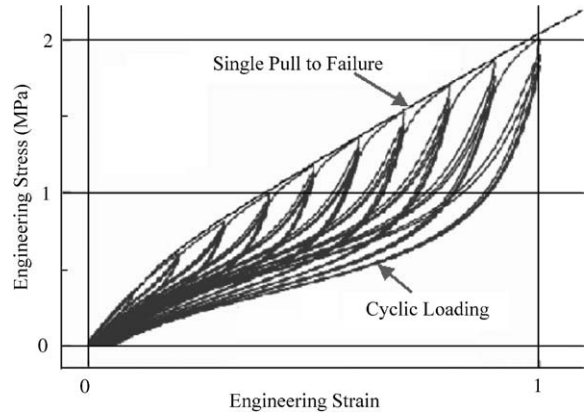


Fig. 3. Test data from cyclic tensioning of rubber specimen.

maximum strain. Firstly, the maximum strain is estimated and the simulation is conducted with the assumed material model to get the maximum strain in the component. If the maximum strain from the simulation is less or larger than the estimated maximum strain, another set of test data with lower or higher maximum strain should be adopted to do curve fitting. If the maximum strain is close to the estimated maximum strain, then no additional iteration is needed and an appropriate material model is achieved. This method is used to build the material model used in the V-ribbed belt simulation. The maximum strain level is taken to be 10%.

In this work, neural network based material model is used for rib rubber. To reduce the computing time, Neo-Hookean material model is chosen for belt cushion rubber and belt back rubber since it is less important to the investigation of the belt pulley contact compared to rib rubber. Fig. 4 shows the curve fitting results for the belt rib rubber compound from neural network method and Ogden strain energy function $N=5$. The neural network has three hidden neurons and the weights and biases are recorded in Table 1. The authors found out that low order strain energy functions such as Neo-Hookean, Mooney, Rivlin, and Ogden strain energy form of $N=1 \sim 4$ all give poor curve fitting results. Ogden energy function $N=5$ gives an acceptable curve fitting to the test data. Even compared with such a high order strain energy function, the neural network still has better curve fitting performance, especially for the equi-biaxial tension and planar ten-

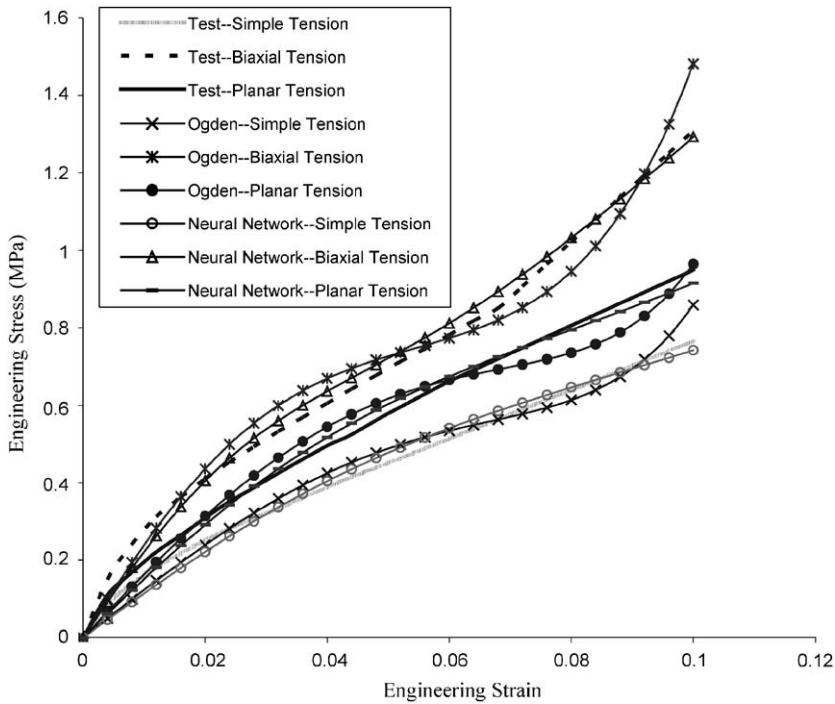


Fig. 4. Predictive and experimental data for rib rubber compound tests.

Table 1
Neural network weights and biases for rib rubber at 23 °C

W_{1i}^h ($i = 1 \sim 3$)	W_{2i}^h ($i = 1 \sim 3$)	W_i^o ($i = 1 \sim 3$)	b_i^h ($i = 1 \sim 3$)	b^o
4.5150	−15.3691	−4.0277	0.07872	3.4878
−25.1595	−34.7927	−54.7941	1.7152	
−2.3159	0.03593	−4.0663	0.08609	

Table 2
Neo-Hookean material constants for cushion and back rubber

	23 °C C_{10} (MPa)	120 °C C_{10} (MPa)	500 h Aging C_{10} (MPa)
Back rubber	6.80450	4.21073	9.12339
Cushion rubber	2.22284	1.75783	2.79909

sion test data. And the neural network based material model is computationally more efficient than the high order Ogden strain energy form. The constants in the Neo-Hookean model for the cushion rubber and back rubber are listed in Table 2.

When V-ribbed belt running on an automotive engine, it subjects to temperature changes due to the environmental effect and the heat from the belt-pulley frictional contact. The mechanical properties of rubber material differ under different temperature. In this

study, the belt rubber compounds are tested under 23 °C, and 120 °C. The simple tension stress–strain curves from experiments are presented in Fig. 5. It can be seen that rubber compounds become softer when they are working under higher temperature. Neural network weights and biases for rib rubber compound working under 120 °C are presented in Table 3. The constants in the Neo-Hookean model for the cushion rubber and back rubber working under 120 °C are listed in Table 2.

A gradual degradation in the mechanical properties of rubber material is observed during its service time. This effect is called aging. In this work, heat accelerated aging of the belt rubber compounds is conducted. The test specimens were kept under 120 °C for 500 h. Then the specimens were tested at room temperature. The simple tension stress–strain curves from experiments are presented in Fig. 5. It is observed that the rubber compounds become stiffer after aging. This may change the pressure on the belt rib and

pulley groove contact interface and hence affect the contact mechanics. Neural network weights and biases for aged rib rubber compound are presented in Table 4. The constants in the Neo-Hookean model for the aged cushion rubber and back rubber are listed in Table 2.

Neural network based hyperelastic material model was then implemented in ABAQUS using the user subroutine—UHYPER. In the subroutine, the user is required to define the strain energy function and first, second and third partial derivatives with respect to strain invariants \bar{I}_1, \bar{I}_2 and volume ratio J . For incompressible material only the first and second derivatives involving \bar{I}_1 and \bar{I}_2 are required. The subroutine is written in FORTRAN. The strain energy and the partial derivatives of the strain energy function are calculated in terms of the first and second strain invariants which are passed in when the subroutine is called. The implemented material model was then tested by simple case studies to simulate the uniaxial tension, equibiaxial extension and planar extension experiments. It was found to give stable performance.

Polyester reinforcing cords are used to strengthen V-ribbed belts. They are much stiffer than rubber compounds and subjected to a small strain. Therefore they are treated as elastic material in the model. Cords properties under different temperature are listed in Table 5.

5. Geometric model, constraints and simulation procedures

A three-dimensional finite element model is required to investigate V-ribbed belt-pulley contact mechanics. To reduce computational time, each pulley in the drive system was classified as either backside flat or grooved pulley and independently analyzed with only a section of the belt (Fig. 6). By varying

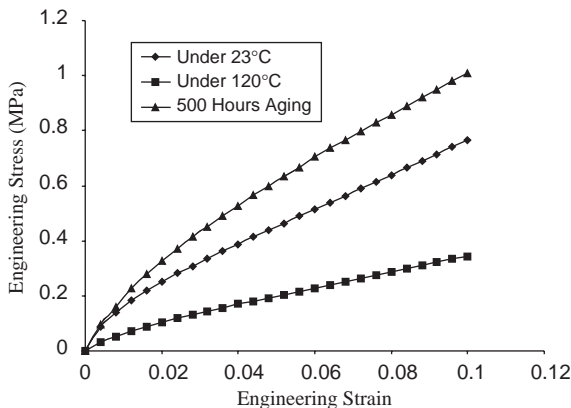


Fig. 5. Experimental data showing the effect of temperature and aging.

Table 3
Neural network weights and biases for rib rubber at 120 °C

W_{1i}^h ($i = 1 \sim 5$)	W_{2i}^h ($i = 1 \sim 5$)	W_i^o ($i = 1 \sim 5$)	b_i^h ($i = 1 \sim 5$)	b^o
−9.5889	3.0822	−0.4222	22.4493	−5.3740
−3.6689	7.4253	0.31490	−10.5720	
−58.8545	38.6802	−0.02737	62.9354	
−11.7854	36.7158	12.4487	−67.9615	
−4.9374	0.086069	−6.8478	22.4543	

Table 4
Neural network weights and biases for rib rubber at 500 h aging

W_{1i}^h ($i = 1 \sim 3$)	W_{2i}^h ($i = 1 \sim 3$)	W_i^o ($i = 1 \sim 3$)	b_i^h ($i = 1 \sim 3$)	b^o
4.2528	−1.0546	3.3488	−11.153	−0.5182
47.674	−53.164	−22.866	10.431	
411.38	−523.50	−35.491	328.10	

Table 5
Cord properties

	Young's modulus E (GPa)	Poisson's Ratio ν
Reinforcing cord 23 °C	8.0	0.3
Reinforcing cord 120 °C	5.387	0.3

pulley diameter, entering and exiting belt span tensions, wrap angle, and pulley horsepower load, each pulley in the drive system can be modeled. All of these parameters were considered boundary conditions to the base model. Only half rib is modeled to further reduce the computational cost. Eight node solid brick elements with hybrid formulation and reduced integration (C3D8RH in ABAQUS) are utilized. Hybrid formulation is used because it has better performance when dealing with incompressible material. Reduced integration is chosen to reduce the computing time. Fig. 7 shows the rib cross-section discretion. Totally 14 elements are used across the half rib section. The modeled belt length is 400 mm. There are totally 300 elements along the belt length. They are unevenly distributed. The elements which will be in contact with the pulley during the simulation are shorter. The length of these elements is about 1.0 mm. Totally 4200 elements are used for the modeled half rib belt segment. This mesh is fine enough to study the contact between the belt rib and pulley groove.

To simplify the applying of the boundary conditions and loads to the belt ends, a rigid plane surface is used to tie boundary elements together. Forces and displacements are added directly to the reference nodes of the rigid plane surfaces and transferred to the belt to control belt tension and pulley rotation angle. The pulley was modeled as a rigid surface by an analytical function and assigned a reference node, which controls the motion of the pulley. Coulomb friction co-

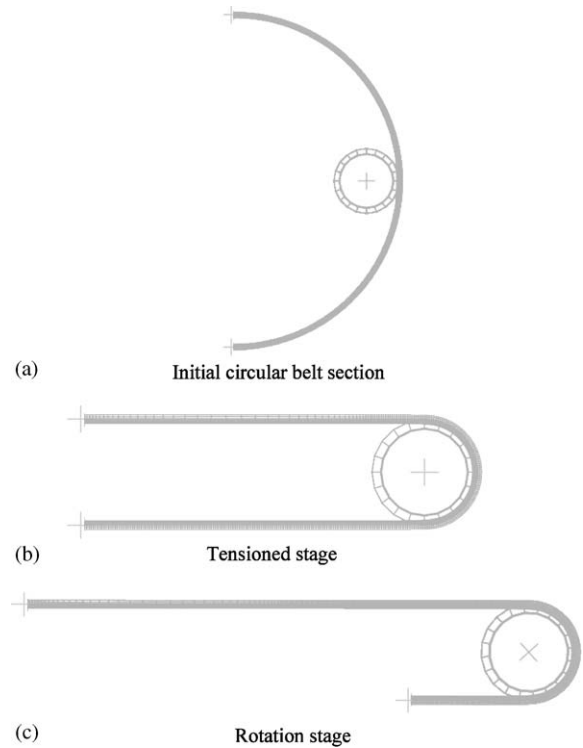


Fig. 6. Simulation stages.

efficient was measured as 0.3 for belt rib and pulley groove contact.

The initial unloaded configuration of the model was a pulley placed inside the circular half loop of the belt, as shown in Fig. 6a. In the first analysis stage the pulley was moved outward without rotating until contact was loosely made with the belt. In the second stage, a concentrated force is applied to the pulley to create the desired total tension in the belt (Fig. 6b). Finally, in the third stage, a torque is applied to the pulley and a force set at one end of the belt to maintain specified tension in each span. A ve-

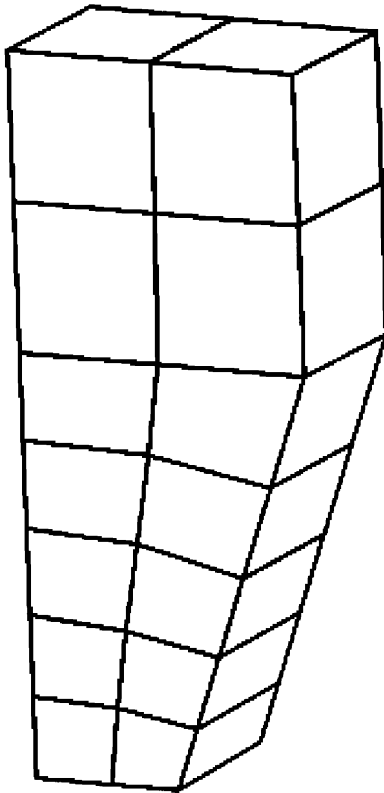


Fig. 7. FEA mesh.

locity is applied to the other belt end to rotate the pulley (Fig. 6c).

6. Results

The FEA model is used to study the belt pulley contact issues such as the slip and stick zone, belt rib seating depth, the contact pressure distribution on the rib surface and rib shear deformation. These issues are closely related to the belt drive performance such as belt transmission efficiency, belt wear and belt fatigue life. They are affected by the belt drive parameters such as pulley diameter, pulley groove profile and belt material properties. These parameters are investigated in this work.

To obtain maximum power capacity and minimum wear, a certain pressure distribution on belt rib is desired. In this distribution the pressure is highest near

the middle of the rib flank and small at the rib tip. The angle of pulley groove profile has large influence on rib pressure. Figs. 8 and 9 shows the pressure distribution on rib surface when it is in contact with pulleys of wedge angle 37° and 39° . The rib wedge angle is 40° . The pulley diameter is 70 mm. A torque load of 0.5 Nm is applied. It is clearly seen that the pulley with wedge angle of 39° generates more evenly distributed contact pressure on the rib surface. For the pulley with wedge angle of 37° , the contact pressure increases from rib tip to rib bottom. Wedge angle of 39° is a better choice to maximize the transmitting capacity for this case. The optimum pulley wedge angle is also affected by the pulley diameter. When the belt curvature increases, i.e., the pulley gets smaller, the belt wedge angle becomes smaller [7]. This is seen from Fig. 10. It shows that with the same wedge angle of 39° , when the pulley diameter changes from 70 to 50 mm, the distribution of contact pressure changes. The highest contact pressure is seen on the rib tip for the pulley of 50 mm diameter. This will lead to fast wear at the belt tip. The change of pressure distribution also leads to the change of slip zone on the rib surface. As shown in Fig. 11, much more slip area is observed for the belt in contact with the pulley of 50 mm diameter. The large slip zone is partially due to the undesirable rib pressure distribution. When designing belt drives, the influence of belt curvature on belt wedge angle should be taken into consideration.

The material properties of the belt components are affected by temperature and aging. When temperature increases, rubber compound and polyester cord both become softer. This causes the change to belt pulley contact pressure, belt shear deformation, belt seating and belt tension distribution. Fig. 12 shows the contact pressure for the belt working under 120°C . Strain from thermal expansion is not considered. The material properties under 120°C are input to the finite element model. The pulley diameter is 70 mm and a torque load of 0.5 Nm is applied. The contact pressure at the rib tip is larger than rib flank. This is different from Fig. 8 which shows the contact pressure for the same belt drive configuration with the material properties under 23°C . A smaller pulley wedge angle may be used to reduce the pressure peak at rib tip.

Rib shear deformation is caused by the friction force generated at belt-pulley contact interface. The frictional contact force is transferred from the belt-pulley

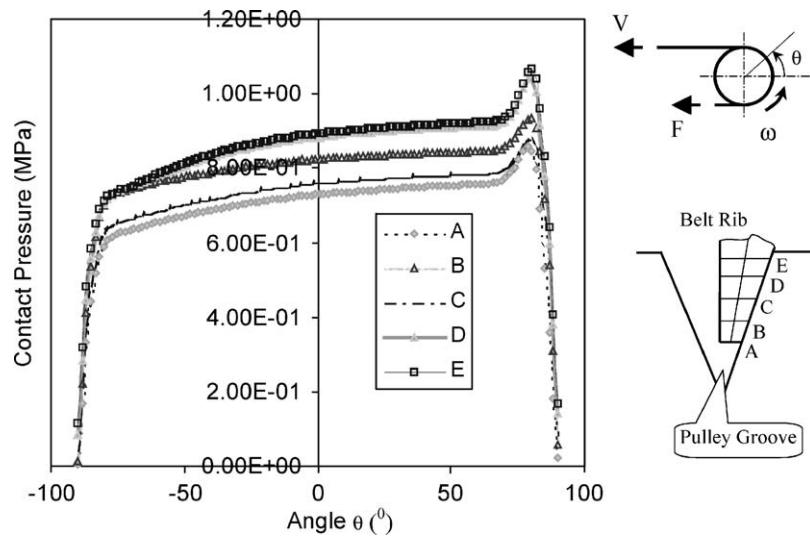


Fig. 8. Distribution of contact pressure (Pulley diameter 70 mm, pulley wedge angle 39°, temperature 23 °C, no aging).

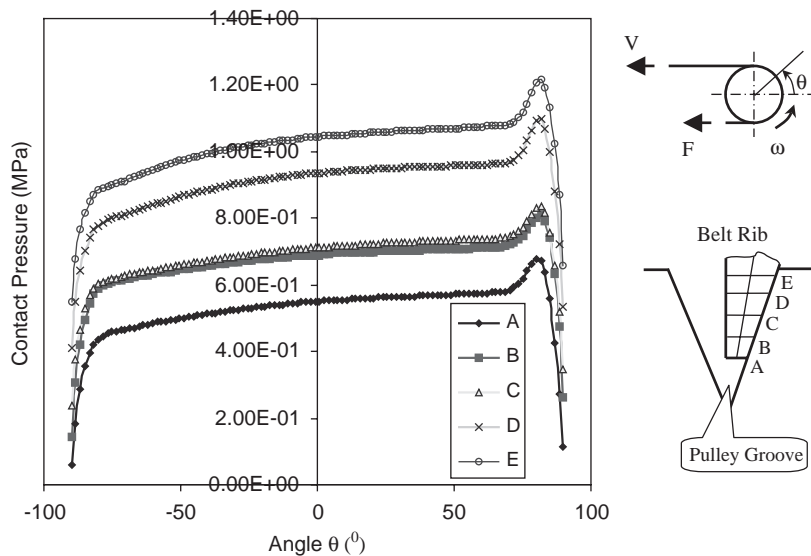


Fig. 9. Distribution of contact pressure (Pulley diameter 70 mm, pulley wedge angle 37°, temperature 23 °C, no aging).

contact interface through the rib rubber to the cord layer and a shear strain is built in the belt. Fig. 13 shows the shear deformation. Shear angle γ is measured from the cord layer to the rib tip. Fig. 14 compares belt rib shear deformation for the belts serving under 23 °C and 120 °C. The large shear deformation

when belt working under 120 °C will cause more speed loss and reduce belt drive transmission efficiency. Because belt materials are softer at higher temperature, belt also has larger radial compliance. Fig. 15 compares the radial position of rib tip nodes at the temperature of 23 °C and 120 °C. The radial position

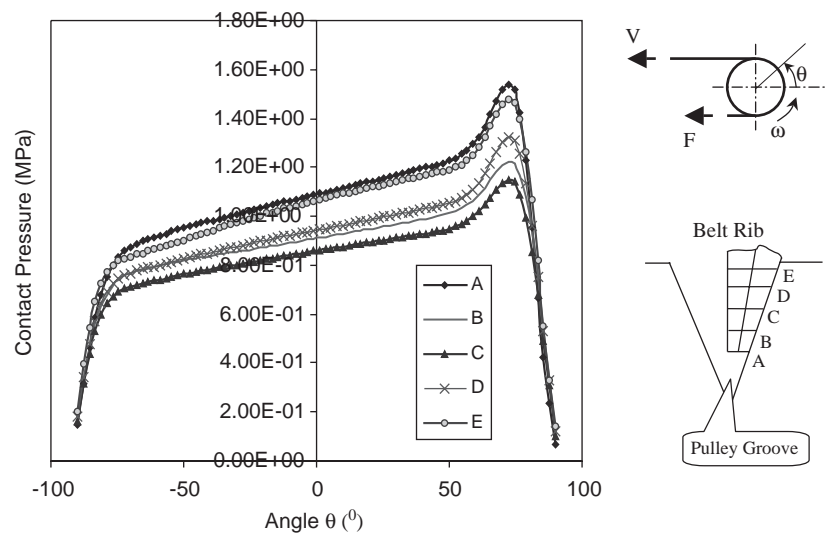


Fig. 10. Distribution of contact pressure (Pulley diameter 50 mm, pulley wedge angle 39°, temperature 23 °C, no aging).

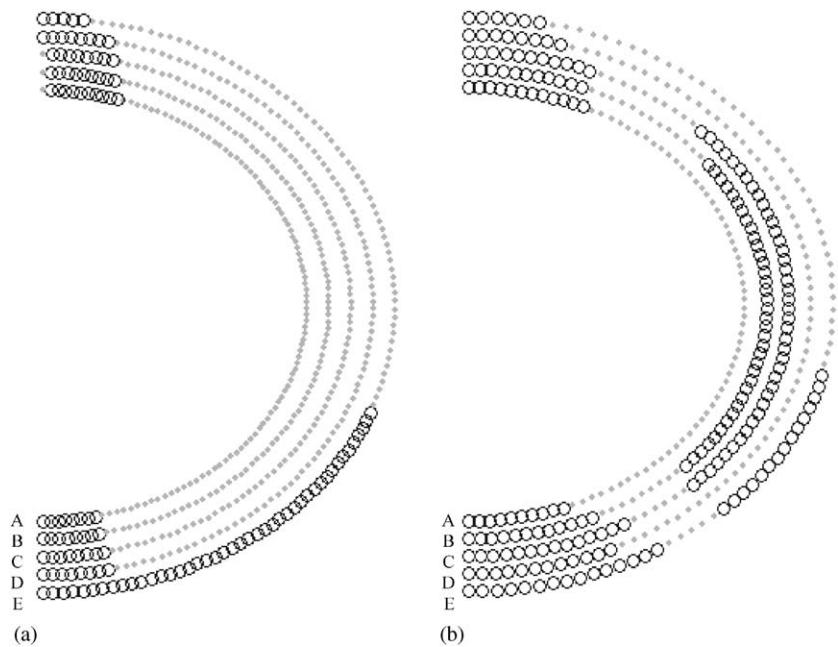


Fig. 11. Effect of pulley diameter on slip zone (circle) on the rib surface in contact with pulley.

sition for 120 °C is smaller than 23 °C, which means that the belt rib seats deeper into pulley groove. This is also a factor contributing to speed loss investigated by Gerbert [5].

Fig. 16 shows the slip and stick zone on the rib surface in contact with the pulley. Slip is found when the belt enters and exits pulley grooves. Both entry and exiting slip zone are much larger for the belts

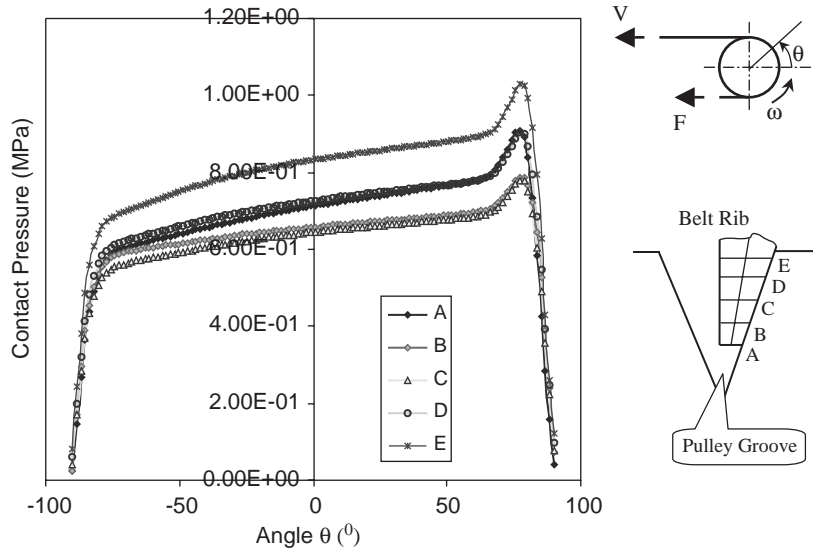


Fig. 12. Distribution of contact pressure (Pulley diameter 70 mm, pulley wedge angle 39°, temperature 120 °C, no aging).

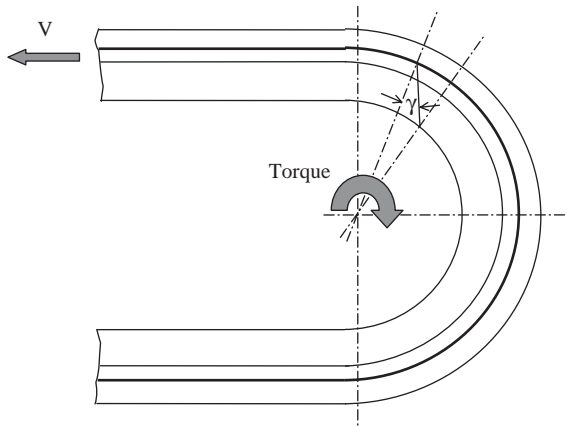


Fig. 13. Shear deformation in the belt.

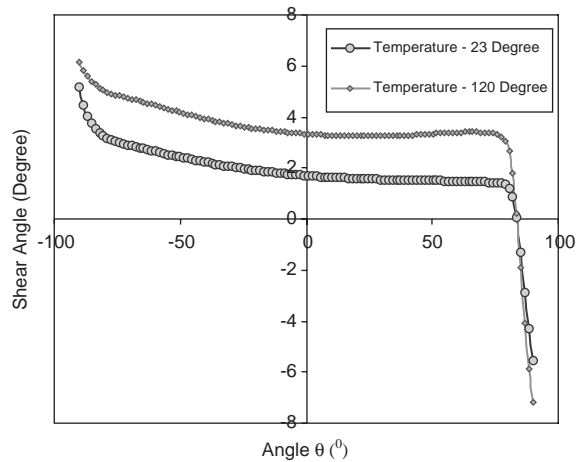


Fig. 14. Shear angle along the belt in contact with pulley groove.

under 120 °C. From the above results, it is clear that temperature has very large influence on belt pulley contact. To reduce the temperature effect, materials less influenced by temperature should be used for the belt components.

Aging causes rubber compounds to change their mechanical properties. Belts become less flexible with aging. Fig. 17 shows the comparison of shear angle for the belts with 500 h aging and without aging. As

expected, the shear angle for the aged belt is less than the belt without aging. This is desirable from the viewpoint of reducing speed loss from shear deformation. But since the aged belt is stiffer, more energy is needed to bend it around the pulley. This causes the efficiency loss referred to as torque loss due to bending by Childs [18]. The energy is transformed into heat and gives harmful effects to the belt. Aged belts also have larger

stresses. As shown in Fig. 18 the normal stress along the belt length at rib tip is higher for the aged belts. The higher stress will accelerate belt fatigue.

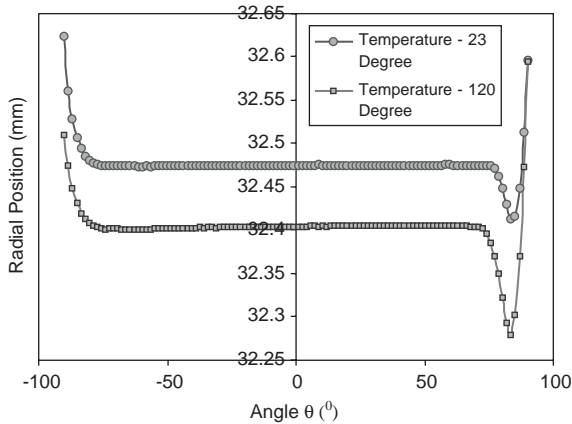


Fig. 15. Radial position of rib tip in contact with pulley groove (Temperature 120 °C).

7. Conclusions

A neural network based hyperelastic material model is introduced. It is found to give better performance than the available strain energy functions. The material model is used to characterize belt rubber and implemented using ABAQUS user subroutine. A three-dimensional finite element model was built to simulate V-ribbed belt front-end accessory drives and study belt pulley contact mechanics such as contact pressure distribution, belt slip and belt shear deformation. It was found that belt and pulley groove wedge angle has large influence on the contact pressure distribution on the rib surface. Belt wedge angle is affected by pulley diameter. Smaller wedge angle is observed when belts bend around a smaller pulley. The properties of belt materials have significant influence on the belt–pulley contact mechanics. Rubber becomes softer when subjected to higher temperature. Belts working under higher temperature seat deeper into pulley grooves and a larger slip zone and larger shear deformation are observed. These factors contribute

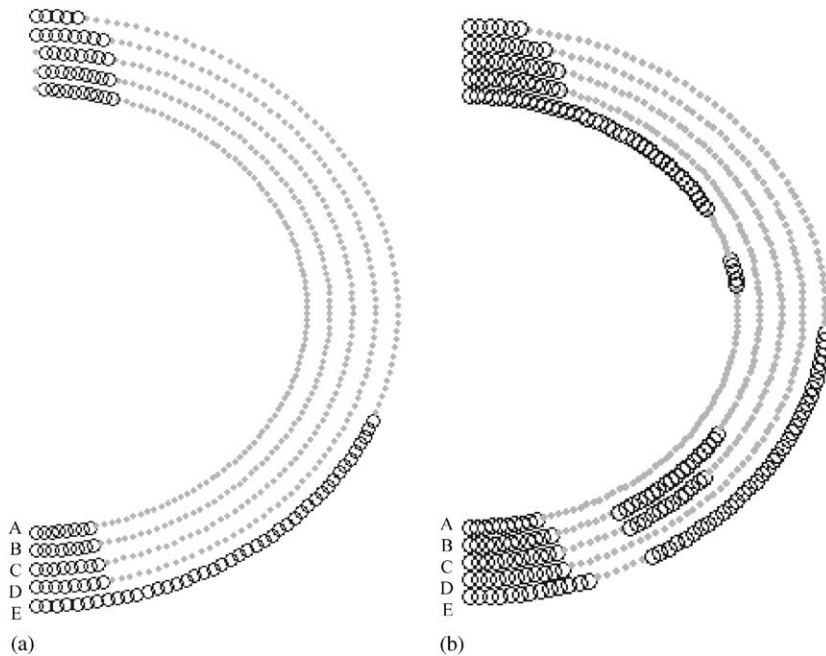


Fig. 16. Effect of temperature on slip zone (circle) on the rib surface in contact with pulley.

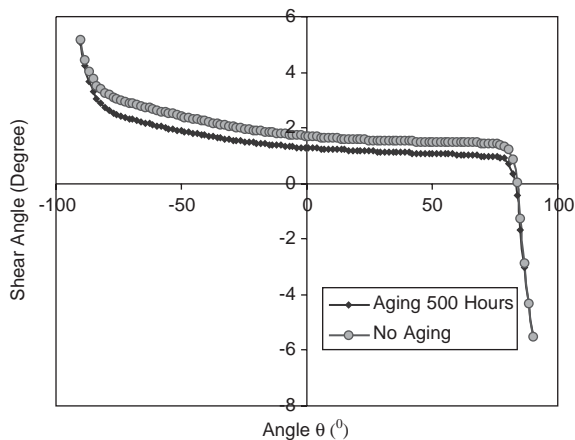


Fig. 17. Radial position of rib tip in contact with pulley groove (Aging 500 h).

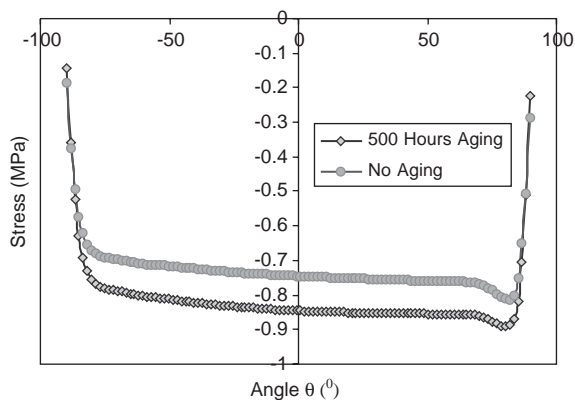


Fig. 18. Normal stress along the belt length at rib tip.

to the loss of belt drive transmission efficiency and increase of belt wear. Aging causes belts to lose some of their flexibility. Larger stress will be generated when the aged belts are bent around the pulley. This will accelerate belt fatigue.

Acknowledgements

This project is sponsored by MarkIV Automotive. The support is gratefully acknowledged.

References

- [1] D. Dowson, History of Tribology, Longmans, London, 1979.
- [2] O. Reynolds, Creep theory of belt drive mechanics, The Engineer 38 (1874) 396–397.

- [3] T.C. Firkbank, Mechanics of the belt drive, Int. J. Mech. Sci. 12 (1970) 1053–1063.
- [4] D.G. Alciatore, A.E. Traver, Multipulley belt drive mechanics: creep theory vs. shear theory, J. Mech. Design 117 (1995) 506–511.
- [5] G. Gerbert, Belt slip-A unified approach, J. Mech. Design 118 (1996) 432–438.
- [6] S. Amijima, T. Fujii, T. Kiji, K. Tani, M. Inukai, Study on the V-Ribbed Belt, Bull. JSME 29 (1986) 2317–2322.
- [7] H. Hansson, Geometry conditions for good power capacity in a V-ribbed belt drive, J. Mech. Design 112 (1990) 437–441.
- [8] D. Yu, T.H.C. Childs, K.W. Dalgarno, Experimental and finite element studies of the running of V-ribbed belts in pulley grooves, Proceeding of the Institute of Mechanical Engineers, vol. 212, Part C, 1998, pp. 343–354.
- [9] S.M. Tabatabaei, T.H.C. Childs, D. Yu, Mechanical performance of V-ribbed belt drives, (experimental investigation), SAE Technical Paper Series, 970006, International Congress & Exposition, Detroit, Michigan, February 24–29, 1997.
- [10] S.M. Tabatabaei, G.H. Payganeh, T.H.C. Childs, Mechanical performance of V-ribbed belt drives, (theoretical modeling), SAE Technical Paper Series, 2001-01-0367, International Congress & Exposition, Detroit, Michigan, March 5–8, 2001.
- [11] J. Connell, L. Rorrer, Friction-Induced Vibration in V-ribbed Belt Applications, ASME DE, vol. 49, Friction-Induced Vibration, Chatter, Squeal, and Chaos, 1992, pp. 75–85.
- [12] C. Sloan, K. Chandrashekhara, W. Breig, L. Oliver, Simulation of V-ribbed belt tracking, SAE Technical Paper Series, 1999-01-0642, International Congress & Exposition, Detroit, Michigan, March 5–8, 1999.
- [13] L.R.G. Treloar, The Physics of Rubber Elasticity, Clarendon Press, Oxford, 1958.
- [14] R.W. Ogden, Nonlinear Elastic Deformation, Dover, New York, 1997.
- [15] ABAQUS, ABAQUS Theory Manual, Hibbitt, Karlsson & Sorensen, Inc., 2001.
- [16] T. Belytschko, W.K. Liu, B. Moran, Nonlinear Finite Elements for Continua and Structures, Wiley, New York, 2000.
- [17] T. Nguyen-Thien, T. Tran-Cong, Approximation of functions and their derivatives: a neural network implementation with applications, Appl. Math. Modeling 23 (1999) 687–704.
- [18] T.H.C. Childs, D. Cowburn, Power transmission losses in V-belt drives, Part 2: Effects of small pulley radii, Proceedings of the Institute of Mechanical Engineers, Part D, vol. 201, 1987, pp. 41–53.

Further Reading

- [19] K. Chandrashekhara, C. Sloan, M. Xu, W. Breig, L. Oliver, Material non-linear analysis of V-ribbed belts, ACS, Rubber Division, 155th Technical Meeting, Chicago, IL, April 13–16, 1999.

- [20] T.H.C. Childs, K.W. Dalgarno, V-ribbed belt design, wear and tracking capacity, Proceedings of the Institution of Mechanical Engineers, Part D, vol. 212, 1997, pp. 333–353.
- [21] T. Lawrence, F. Wilson, Verified predictive design of poly-V[TM] belts using ABAQUS/explicit, Presented at the 10th UK ABAQUS User Group Meeting, TWI, Arlington, Cambridge, UK, September 21, 1995.
- [22] D. Yu, T.H.C. Childs, K.W. Dalgarno, V-ribbed belt design, wear and tracking capacity, Proceedings of the Institute of Mechanical Engineers, vol. 212, Part D, 1998, pp. 333–344.